Lecture 2 ARRAY LAYOUT SOURCE INVERSION

Subject 1 Relationship between Strong-Motion Array Parameters and the Accuracy of Source Inversion and Physical Waves

1. INTRODUCTION

In several regions where large earthquakes are expected to occur in the near future, immediate installation of dense strong-motion arrays was strongly recommended at the International Workshop on Strong-Motion Earthquake Instrument Arrays held in Honolulu, Hawaii, in 1978 (Iwan, 1978). In spite of the general recognition of the importance for planning strong-motion array layouts, a systematic analysis has never been tried to obtain a relationship between the array layout and the accuracy of source inversions. Also, relatively large inconsistencies were seen among the inversion results for the 1979 Imperial Valley earthquake (e.g., Olson and Apsel, 1982; Hartzell and Heaton, 1983; Archuleta, 1984; Anderson and Silver, 1985), which has provided so far the best available set of strong-motion data and generated a great deal of interest on the limitations of source inversion.

Although there are several objectives in strong-motion array observations, we try to determine how we should distribute seismic array stations for determination of the spatial distribution of moment on a large fault. The major goal of this study is to prepare guidelines for future installations of strong-motion arrays. This study addresses the limitations of current source inversion studies posed by the configuration of the strong-motion array and the number of stations. We apply a modified version of the method previously developed in Miyatake *et al.* (1986) to several synthetic rupture models and evaluate contributions of various types of seismic waves.

An important aspect to be discussed is the contribution of each of the main physical waves to the accuracy of source inversion. A proper answer for this question sheds light on strong-motion array designs. For example, Menke (1985) showed, in his inverse Radon transform/tomographic construction technique, that a complete suite of the far-field observations did not span the complete set of possible projection lines. Near-source data from the 1985 Michoacan, Mexico, earthquake may suggest usefulness of near-field terms (e.g., Anderson *et al.*, 1986; Mendosa and Hartzell, 1989). However, a general argument on the relative significance of various physical waves for source inversion has not been made. We attempt to give an answer by measuring degration in the accuracy of source inversion when various wave types are removed from the problem.

In recent typical inversion studies (e.g., Hartzell and Heaton, 1983; Mori and Shimazaki, 1985), the entire fault is divided into many subfaults, and the slip is allowed to take place on each subfault at a prescribed time point or at a time window consisting of a few prescribed time points; the rupture propagation is basically assumed. Also, a functional form of moment release on each subfault is assumed. The unknowns are parameters associated with the seismic moment on each subfault. In our analysis, we will use a similar parameterization for the representation of an earthquake source process.

In a previous paper (Miyatake *et al.*, 1986), we developed a method to estimate the standard deviation of subfault moment. Assuming a strike-slip fault located at the center of a circular array with *Ns* uniformly distributed stations within a large radius, *R*, the maximum standard deviation normalized by the moment is obtained as

$$\sigma \propto Ne^2 \cdot 10^{R/5}/Ns$$

---

* This lecture note is based on the paper of the same title written by Masahiro Iida, Takashi Miyatake and Kunihiko Shimazaki, published on "Bulletin of the Seismological Society of America, Vol. 80, No. 6, pp. 1533-1552, December 1990".

where Ne is the number of subfaults. In this simulation, only far-field S waves were considered. In the present study, we systematically examine more general cases and include not only far-field S waves, but also near-field terms and surface waves. It will be shown that, when exact solutions in an elastic half-space are used, a different result $\sigma \propto Ne^2/Ns^{1/2}$ holds. σ does not show a simple dependence on R

After briefly reviewing our method in the next section, assumed fault-array geometries are described. We treat three typical types of situations: strike-slip, dip-slip, and offshore subduction thrust faults. The latter two have identical fault geometries, but the station distribution is different. The results of systematically varying fault and array parameters are described, and contributions of far- and near-field terms and surface waves are investigated. They are also interpreted from an array layout point of view.

2. METHOD

Since our method has been fully explained in Miyatake *et al.* (1986), we will briefly summarize the method and give a few comments from an inverse theory point of view. Major differences between our approach and typical methods of source inversion will be distinguished.

As was previously discussed, the entire fault is divided into many subfaults; the slip is allowed to take place only once on each element of the fault. We assume a point source at the center of each subfault with a common source time function, which depends on the subfault size The parameters chosen as the unknowns are the seismic moment and the rupture onset time for each subfault. The known parameters whose uncertainties are taken into account are the dip angle, the strike direction, and the slip angle of each subfault. We consider variable timing errors. It is also assumed that the observed displacement waveform contains errors. All of the errors are assumed to be normally distributed, and their standard deviations are listed in Table 1.

TABLE 1
STANDARD DEVIATIONS OF INDEPENDENT VARIABLES IN ESTIMATING THE SEISMIC MOMENT AND THE RUPTURE ONSET TIME OF SLIP AT EACH SUBFAULT

Dip angle	10.0°
Strike direction	10.0°
Slip angle	10.0°
Wave amplitude	0.01 cm

Exact solutions (Kawasaki *et al.*, 1973) are treated in a semi-infinite homogeneous space. In the previous study (Miyatake *et al.*, 1973) are utilized only far-field S waves. For general applicability of the results, we normalize all the variables as shown in the previous study. For example, the fault length is used to normalize the distances. An introduction of a specific crustal structure would make the results more realistic, but would destroy this normalization scheme. More realistic analysis, which considers a regional-layered structure, will be given elsewhere (Iida *et al.*, in preparation).

We have made two minor changes in going from far-field S waves to exact solutions. First, we use a ramp function because of the simplicity and reduced computation time instead of a slightly more complex function described in the previous study (Miyatake *et al.*, 1986). Second, instead of constant timing errors used in the previous study, variable timing errors of $\delta t = |\delta v/v| \cdot t$ are intuitively introduced, where t is measured after the rupture origin time, v is the wave velocity, and δv is the error in the velocity. Here, $|\delta v/v|$ is set equal to 0.05 on the basis of a few simulations. This assumption signifies that our confidence in properly identifying an arrival in the records as being due to structural disturbance (e.g., interference with different phases and distorted waveform) decreases, the greater the arrival time and the epicentral distance.

The theoretical waveform is a function of both the unknown and known parameters. Denoting by $a_k (k = 1,\ldots,p)$ and $x_l (l = 1,\ldots,q)$ the unknown and known parameters, respectively, the theoretical displacement of the ith station at the jth time point can be expressed as $f_j^i(x_{1ij},\ldots, x_{qij}; \alpha_1,\ldots, \alpha_p)$. We define two residuals as the differences between the observed and estimated values for dependent and independent variables,

$$\begin{aligned} R_{ij} &= F_j^i - f_j^i \\ R_{kij} &= X_{kij} - x_{kij} \end{aligned} \tag{1}$$

where F_j^i and X_{kij} indicate the observed displacement and the true value of the kth parameter of the ith station at the jth time point, respectively. We seek a solution that minimizes the weighted sum of the squares of the two kinds of residuals,

$$S = \sum_i \sum_j (w_{ij} R_{ij}^2 + \sum_k w_{kij} R_{kij}^2). \tag{2}$$

The weights, w_{ij}, w_{kij}, are defined as the reciprocals of the variances (i.e., the squares of the uncertainties listed in Table 1). From the minimization,

$$\delta S = 0, \tag{3}$$

the normal equations can be obtained that can be schematically written in matrix form,

$$C \cdot A = B \tag{4}$$

where an element of matrix $A(A_k)$ indicates the difference between the value of unknown parameter, a_k, and its initial guess a_{k0} (i.e., $A_k = a_{k0} - a_k$) Elements of matrices B and C are expressed as follows,

$$\begin{aligned} B_k &= \sum_i \sum_j \frac{\partial R_{ij}}{\partial a_k} \cdot \frac{R_{ij0}}{L_{ij}} \\ C_{mn} &= \sum_i \sum_j \frac{\partial R_{ij}}{\partial a_m} \cdot \frac{\partial R_{ij}}{\partial a_n} \Big/ L_{ij} \end{aligned} \tag{5}$$

where

$$\begin{aligned} L_{ij} &= \frac{(\partial R_{ij}/\partial f_j^i)^2}{w_{ij}} + \sum_k \frac{(\partial R_{ij}/\partial x_{kij})^2}{w_{kij}} \\ R_{ij0} &= F_j^i - f_j^i(X_{1ij}, \ldots, X_{qij}; a_{10}, \ldots, a_{p0}). \end{aligned}$$

Following Wolberg (1967), the uncertainty of the kth unknown parameter can be assessed without solving

the normal equations, but by an inverse of the C matrix in the normal equations,

$$\sigma a_k^2 = C_{kk}^{-1}. \tag{6}$$

This technique called "prediction analysis" is more advantageous than a Monte Carlo simulation because we need to take the inverse only once for each set of array station locations and the target fault with an assumed rupture mode.

This procedure corresponds to obtaining a covariance matrix of the solution in inverse theory [e.g., equation (44) in Tarantola and Valette, 1982]. However, note that there are no additional constraints to stabilize the solution in equation (3). In many source inversions, the fault is partitioned into a large number of small subfaults. Instability arises due to the ill-conditioned matrix of synthetics, even in an overdetermined system of equations and when the number of subfaults is small (e.g., Hartzell and Heaton, 1983). To stabilize the solution, additional constraints are usually given, such as moment minimization, smoothing, and filtering of singular values. By the stability constraints, the resolution of the solution is sacrificed. In general, it is necessary to compromise two quantities (e.g., Backus and Gilbert, 1967): resolution and variance of the solution.

In the present study, no attempt is made to stabilize solutions. Instead, we require the "perfect" resolution of the solution (i.e., the resolution matrix is an identity matrix). We use only variance to estimate the accuracy of the inversion This is simply because it is desirable to use only one parameter to evaluate the effectiveness of a strong-motion array. Also, it would be extremely time consuming to choose an optimal parameter to obtain a satisfactory tradeoff between resolution and variance, which makes it impossible to estimate each array resolving power for many suites of fault-array geometries owing to an excessive computational burden. Furthermore, a comparison between two cases with different optimal parameters would be difficult.

The predetermined subfault size is important in our study because it gives the spatial resolution. In many source inversions, the subfault size is rather insignificant because the effective resolution is larger than the subfault size It is unfortunate that the resolution of the solution is rarely explicitly described in most source inversions.

Because we only use a linear inversion scheme, errors in estimating the rupture onset time are considerably underestimated. This means that we obtain variance estimates for a locally linear region around the correct rupture onset time in a nonlinear problem, since the ground motions are a nonlinear function of the onset time. Thus, the estimated uncertainty of the onset time will not be used in the following and the accuracy of the source inversion will be evaluated by the maximum standard deviation of subfault moment. Actually, we will use the maximum standard deviation normalized by the moment. Our treatment corresponds to most of typical source inversion schemes in which an *a priori* rupture time distribution is assumed.

Certainly, recent studies have tried to address various approaches for solving nonlinear problems (e.g., Beroza and Spudich, 1988; Olson and Anderson, 1988; Hartzell and Iida, 1990). However, the validity of each method has not yet been justified by sufficient demonstration studies. Some methods depend heavily on the given initial values while others do not use realistic Green's functions. Rather, they seem to be in the process of development. Incorporation of such a nonlinear scheme into our method leads simply to an excessive computational burden in our problem of treating many fault-array combinations. In the current situation, we avoid nonlinear formulations.

3. EXAMINATION OF FAULT AND ARRAY PARAMETERS

Three different geometries are used in this study. Figure 1 shows a pure strike-slip fault with a dip angle, $\delta = 90°$ or a pure dip-slip fault with $\delta = 30°$ located at the center of a circular array. The two faults have the same depth

on the upper edges. Figure 2 shows the second case in which the stations are distributed only in a fan-shaped area. The fault is located at the center of the fan. This case is used for investigating effects of variations of azimuthal coverage of the source and rupture direction. The third case corresponds to an offshore subduction thrust (Fig. 3). Stations are mainly distributed along the coast, but a few OBS stations are tested. Throughout the simulations, all the distances are normalized by the fault length. All the standard values assumed are summarized in Table 2. These fault-array parameters are changed separately to estimate their influence on the inversion uncertainty.

TABLE 2
STANDARD VALUES OF FAULT-ARRAY AND MEDIUM PARAMETERS USED THROUGHOUT SIMULATIONS

Fault Parameters	
Number of fault elements, Ne	18 (=6 × 3)
Aspect ratio (fault width divided by fault length), Φ	0.5
Dip angle for strike-slip fault	90°
Dip angle for dip-slip fault	30°
Depth of the top of the fault, h	0.1
Rupture mode (rupture velocity is fixed at 0.8)	Unilateral
Array Parameters	
Number of stations, Ns	6
Array radius, R	2.0
Azimuthal coverage of the source, ϕ	360°
Components used	All components
Medium Parameters	
P-wave velocity, V_p	1.71
S-wave velocity, V_s (normalized by this value itself)	1.0
Density, ρ(normalized by this value itself)	1.0

3.1 Fault parameters

Five parameters are considered: (1) the number of subfaults on the fixed fault, Ne; (2) the aspect ratio -- Φ = the fault width divided by the fault length (the area of the subfaults is fixed); (3) the dip angle, δ; (4) the fault depth, h; and (5) the rupture mode. Strictly speaking, some of the fault parameters are closely related, and each of them cannot be changed separately. For example, such a relationship exists between the number of subfaults and the aspect ratio. This is because all the distances are normalized by the length of the entire fault, and the fault length has to be kept unchanged. Thus, only the fault width has to be changed to investigate the effect of the aspect ratio. In simulation (1), to estimate the spatial resolution of the source inversion, the number of subfaults and the subfault size are changed while the size of the entire fault is unchanged. Two different subfault shapes are used, a square element and a rectangular one whose length is twice its height. In simulation (2), both the number of subfaults and the aspect ratio are changed, while the subfault size and the number of subfaults in a row along the strike direction are unchanged. In this case, the fault width and the entire fault area increase when the number of subfaults increases, because the fault length is kept unchanged. For investigating the effect of the rupture mode, four cases are considered: unilateral rupture, bilateral rupture, rupture that starts from the shallower side and propagates downward, and rupture that starts from the deeper side and propagates upward.

3.2 Array parameters

Four parameters are considered: (1) the number of stations, Ns; (2) the array radius, R; (3) the azimuthal coverage of the source, ϕ, defined as the circumferential angle of a fan in which stations are distributed; and (4) the components of the seismograms. In simulation (3), the azimuthal coverage of the source, a different type of array is used (as shown in Fig. 2). The stations are distributed randomly in the dan-shaped area with a radius of 2.0. Two cases of unilateral rupture (in opposite directions) are assumed. Furthermore, we consider two cases as

follows, because *Ns* and ϕ can be interrelated. In the first case, the number of stations, *Ns*, is kept constant, but the density of stations is changed according to a change in azimuthal coverage, ϕ. In the second case, the number of stations, *Ns*, is kept proportional to the azimuthal coverage, ϕ. In this case, the density of stations is constant. For simulation (4), for the components of the seismograms, we will examine the following seven cases: (1) only the component parallel to the fault strike (the first component) is used; (2) only the horizontal component perpendicular to the fault strike (the second component); (3) only the vertical component (the third component); (4) both the first and second components; (5) both the first and third components; (6) both second and third components; and (7) all the three components.

3.3 Simulation for an offshore subduction thrust

Land stations are not necessarily effective to investigate the rupturing process of offshore events. However, no quantitative arguments on whether strong-motion ocean bottom seismographs are worth installing have yet been made. We attempt to demonstrate or refute their necessity by conducting a test of the relative value of ocean bottom seismographs and surface ones for studying the rupture of a subduction zone event.

At present, a semi-permanent strong-motion ocean bottom seismograph does not exist, although temporary networks of strong-motion ocean bottom seismograph systems are in the process of development. Since 1978, relatively low-cost seismic stations for measuring strong ground motion on the ocean bottom have been tested (Steinmetz *et al.*, 1979, 1981). The strong-motion ocean bottom seismograph system was constructed by extending and enhancing design concepts employed in the development of a high-gain OBS (Latham *et al.*, 1978). These experiments indicate that an ocean bottom station is capable of recording ground accelerations up to about 1.0 *g*, in the 0.1 to 10 Hz frequency band, with good reliability in most cohesive type soil conditions.

For this simulation, a fault and array geometry shown in Figure 3 is used. The numbers of surface stations and ocean bottom stations, *Ns* and *No* are varied separately to estimate their influence. The distribution in the surface stations is dependent upon only the number of surface stations, *Ns*, and the positions are fixed as illustrated in Figure 3. Several patterns of ocean bottom stations are tested for each pair of *Ns* and *No*. They are intended to determine the best station positions.

4. RESULTS

4.1 Fault parameters

Effects of the fault parameters are summarized in Figure 4, where a and b show that the normalized uncertainty, σ is roughly proportional to Ne^2 (the number of subfaults on the fixed fault) and Φ^2 (the aspect ratio: the fault width divided by the fault length). The number of subfaults, *Ne*, can be easily substituted by the subfault size (the spatial resolution). The two relationships simply represent the identical effect because Φ is proportional to *Ne* in simulation (2). On the other hand, the uncertainty is almost independent of the fault mechanism. The uncertainty depends little on the dip angle (Fig. 4c). Also noticeable in Fig. 4a is that square fault element gives a better result than a rectangular one. This is probably because the rectangular case requires greater depth resolution. The results in Figure 4c showing larger uncertainty for a steeper fault plane suggest that depth resolution is worse than resolution in the horizontal direction.

Figure 4d indicates that effects of the fault depth are not as large and not as simple. Please note that the ordinate is in linear scale in Figure 4d and e. In the case for the strike-slip fault, the accuracy is unaffected by fault depth. However, for the dip-slip fault, the accuracy becomes low when $h = 0.5$ to 1.0. We find that the accuracy is nearly independent of the rupture modes (Fig. 4e).

4.2 Array parameters

The uncertainty, σ, is found to roughly obey an inverse root dependence on *Ns* (Fig. 5a). Together with the number of subfaults, *Ne*, a relationship $\sigma \propto Ne^2/Ns^{1/2}$ suggests that numerous stations are required to analyze the detailed rupturing process (i.e., the generation of high-frequency seismic waves). Figure 5b exhibits that the inversion uncertainty becomes minimum when the array radius, *R*, is around 0.75 to 2.0 times the fault length. The large

array radius is effective perhaps because of the presence of surface waves. We will elaborate on this observation later.

The simulation on station azimuthal coverage shows that $\sigma \propto \phi^{-1}$ holds approximately in the case where Ns is kept proportional to ϕ (Fig. 5c) Please note that $\sigma \propto Ns^{-1/2}$ holds when the azimuthal coverage is unchanged. Thus, the relationship $\sigma \propto \phi^{-1}$ under the condition of $\sigma \propto Ns$ shows a remarkable contribution of azimuthal coverage. Here, the relationship is determined by the case where the rupture direction is considered disadvantageous for the station array (i.e., the rupture propagates toward the station array, Case *A*). When the rupture propagates away from the station array, the accuracy of the solution loses dependence on the azimuthal coverage of the source. Apparently, good azimuthal coverage largely enhances the ability to separate arrival times between seismic waves. Figure 5d shows that the horizontal component parallel to the fault strike tends to contribute to a strike-slip fault, and the vertical component to a dip-slip fault.

4.3 Simulation for an offshore subduction thrust

Effects of the increasing numbers of surface stations and ocean bottom stations on the inversion uncertainty are displayed in Figure 6. Interestingly, the inversion uncertainty does not appear to saturate as the number of surface stations is increased in the absence of ocean bottom stations. The graph suggests that effects of ocean bottom stations are not very dramatic. For example, even if we increase the number from 1 to 2 or from 2 to 4, the large drop in the inversion uncertainty is not seen. In order to recover the accuracy of the source inversion equivalent to that attained by using four ocean bottom stations (together with four surface stations), we have only to install 14 additional surface stations. In this case, one OBS is worth about four surface stations. Considering difficulty in the design, deployment and maintenance for ocean bottom instruments, it is doubtful that our results are a strong incentive to deploy permanent ocean bottom stations in subduction zones.

The simulation also gives an interesting view concerning positions of ocean bottom stations. As seen in Figure 6, if we have only one instrument, it should be located on the opposite side to the land about the fault, not within the fault zone. In the case of two instruments, one should be deployed on the opposite side to the land while the other is within the fault zone above the fault. This indicates that azimuthal coverage is more important than proximity to the fault

4.4 Discussion

The result $\sigma \propto 1/Ns^{1/2}$ suggests that just an increase in the number of stations is not sufficient to investigate the detailed fault rupturing process. Instead, array stations should be deployed accounting for the effectiveness of an array layout. This can be seen by comparison with the result of $\sigma \propto 1/\phi$, which has been obtained under the condition of $\phi \propto Ns$, showing the primary importance of azimuthal coverage of the source. Also, in accordance with Figure 5b showing σ versus R, the appropriate array-radius ranges are around 0.75 to 2.0, reflecting the usefulness of distant stations regardless of the fault type. Potentially more important are results derived from a simulation on an offshore subduction thrust. They tell us how the accuracy of the source inversion is controlled by the relative numbers of surface and ocean bottom stations and where the ocean bottom stations should be installed. Our results do not appear to show convincingly that permanent ocean bottom stations are needed in subduction zones.

In a previous study (Miyatake *et al.*, 1986), we obtained, using only far-field *S* waves and the same array stations as those in this study, an empirical relationship among the maximum standard deviation, σ, and three basic parameters for a strike-slip fault.

$$\sigma \propto Ne^2 \cdot 10^{R/5}/Ns$$

As previously discussed, the results of the present study differ with the aforementioned results, especially concerning the dependence of the inversion uncertainty on the array radius, R. In the previous study, effects of smaller array

radius on the inversion uncertainty were not examined. We should note that the inversion uncertainty increases when the array radius is smaller than the fault length (Fig. 5b; also see Fig. 11 for the far-field *S*-wave case); therefore, the empirical relationship obtained in the previous study should be restricted to ranges greater than the fault length. Moreover, different trends are seen in the range of large array radius between the current and previous studies, as shown in Figure 5b.

When we use exact solutions, the accuracy of the source inversion is more independent of most parameters than in a previous study of only far-field *S* waves (iida *et al.*, 1986) except for the number of subfaults, *Ne*. Dependence of the inversion accuracy on most parameters is rather similar regardless of the seismic waves employed, exact solutions, or only far-field *S* waves, except for two parameters, the fault depth, *h*, and the array radius, *R*. We infer naturally that the difference originates from surface waves (Rayleigh waves) since the two parameters are related with them. Thus, the simultaneous use of different seismic waves causes the solutions to be insensitive to array configuration. In contrast, the dependence of the inversion uncertainty on the number of subfaults is not connected to what sorts of seismic waves are employed.

Through a series of simulations, however, we have not referred to effects of array configuration in this paper as it is difficult to parameterize. Our studies (Iida *et al.*, 1988; Iida, 1990), which attempted to determine optimum strong-motion array geometry for source inversion, using either only far-field *S* waves or complete Green's functions in a homogeneous half space, indicated that the most preferable array involves two different kinds of stations: stations close to the fault and aligned parallel to its strike, and stations surrounding the fault area with good azimuthal coverage. The former stations resolve the latter stage of the rupturing process while the latter stations resolve the earlier stage. In the two studies, three typical types of faults were chosen. The array geometries obtained in the latter study (Iida, 1990) were consistent with those proposed on the basis of empirical judgement at the 1978 International Workshop (Iwan, 1978).

5. PHYSICAL WAVES

There are two problems to be addressed. How can we extrapolate the idealized array geometries utilized in this study to those that can actually be used in the field? The other problem is the adequacy of the half-space approximation postulated throughout our study. There also seems to be two major differences between the real earth structure and the homogeneous half-space: (1) the half-space has no Love waves, and (2) the half-space model may not be a good one in terms of body waves that leave the source downgoing and are observed at distant stations.

If we understand physical processes that produce our results, we may be able to solve these problems. It would be very helpful to show which physical waves contribute more to the accuracy of the source inversion in the half-space model. We could investigate effects of far- and near-field terms as well as surface waves by removing them from the problem. In our attempt to separate surface waves, we initially applied a phase-velocity filter to half-space seismograms (Spudich and Ascher, 1983), but this did not work well because of the similarity of *S* and Rayleigh wave velocities. Ultimately, we chose to substantiate surface-wave effects by comparing half-space seismograms and wholespace ones. We were unable to find a technique to separate far- and/or near-field terms in half-space seismograms. This separation is straightforward for wholespace seismograms. We will examine effects of far- and near-field terms in the wholespace (e.g., Aki and Richards, 1980). We use the definition of near-field terms used by Hasegawa (1975). This means that intermediate terms, named by Aki and Richards, are included in our near-field terms.

Inclusion (removal) of far- and near-field terms and surface waves (Rayleigh waves) has two contrasting effects. It will complicate (simplify) the waveform by interference with different phases and result in an increase (a decrease) in the uncertainty of the solution. On the other hand, an increase (a decrease) in the source information contained in the waveform will decrease (increase) the uncertainty. Two factors to be examined on physical waves may be dip angle and fault depth: dip angle is related to the relative separation in arrival times between seismic waves radiated from subfaults while a shallow fault depth causes preponderance of surface waves. In the following physical wave simulations, we have changed the number of subfaults from 18 to 8 for computational expedience,

and have reduced the rise time form 0.58 to 0.33. These two changes reduce source complexity, so that effects of physical waves will be emphasized. Two sorts of simulations will be performed.

5.1 Phase interference and source depth

The fault-array layout for the first simulation is a slightly modified version of Figure 1 and is shown in Figure 7. Stations 1 to 3 are shifted toward the center of the station array in order that the distance between each station and the array center is halved, thereby emphasizing the near-field terms. The three types of fault geometries used are summarized in Table 3. The first two are exactly the same as used in most simulations. The third one is appended for two purposes. Comparing results for the first model fault plane with those for the third one with the same average fault depth, we can derive the effects of phase interference due to the relative separation in arrival times between seismic waves. We measure the phase interference by $PI \equiv \Sigma^{Ns}_{i=1} (t_{ri}-t_{si})/Ns$, where t_{ri} and t_{si} are the arrival times of the latest Rayleigh wave and the earliest S wave observed at the ith station. The calculated values are listed in Table 3. A small PI means large phase interference due to the fault geometry. The effects come originally from dip angle. The first fault plane with a 90° dip will produce more severe phase interference than the other two planes because arrival times between various seismic waves radiated from subfaults are very close to each other at all the stations. Also, comparison of results for the fault planes of (2) and (3) will demonstrate effects of surface-wave dominance due to sources with different depths. The types of physical waves used at each station are illustrated schematically in Figure 8 The same 10 cases are tested for each of the three fault planes. Important comparisons among others are those of cases (1) and (3) for surface waves, cases (2) and (5) for near-field terms, and cases (4) and (10) for far-field terms.

TABLE 3

THREE TYPES OF FAULT GEOMETRIES USED TO STUDY EFFECTS OF VARIOUS PHYSICAL WAVES

Type	Slip Direction	Dip Angle	Average Depth of Fault	PI
1	Strike slip	90°	0.35	1.02
2	Dip slip	30°	0.225	1.17
3	Dip slip	30°	0 35	1.13

Parameter, PI, is introduced to measure phase interference due to the fault geometry See text for definition

The accuracy of the source inversion for every case is summarized in Figure 9. At first glance, we find that results for the fault planes of (2) and (3) show a different trend from those for the fault plane of (1). In the fault planes of (2) and (3), primarily surface waves at distant stations contribute to the source inversion [see small uncertainty in cases (1), (2), (5) and (8)]. Secondly, far-field terms are a main contributor in the absence of surface waves at distant stations [see large uncertainty in cases (9) and (10)], whereas near-field terms are not. Our "contribution" means the increase in the source information due to various waves minus the decrease in the effective information due to phase interference. Therefore, no change in the value may imply a comparable increase in the source information and phase interference. Rigorously speaking, contributions from surface waves cannot be complemented by any other waves. Use of the shallower fault (2) identical to fault (3) shows that a predominance of surface waves improves the uncertainty Please note remarkable decrease in the inversion uncertainty in moving from (3) to (2) in cases (1), (2), (5) and (8) in contrast to small changes in cases (3), (4), (6) and (7). Significant decrease in cases (9) and (10) is probably due to large dependence of near-field terms on the hypocentral distance. On the other hand, no improvement can be made with respect to surface waves in the case of vertical fault plane (1). This is primarily due to phase interference. Please note that case (7), where only far-field waves are used, gives the best result We can see that the far-field terms at both near-source and distant stations [see large uncertainty in cases (8) to (10)] control the inversion uncertainty more strongly than the near-field terms. Our first simulation tells the significance of avoiding phase interference.

5.2 Physical waves and array radius

To investigate a relationship between the accuracy of the source inversion and the array radius for different physical waves, we conduct the second simulation that again uses the fault-array layout shown in Figure 1. Physical waves examined include: (1) a complete half-space solution; (2) a complete wholespace solution; (3) only far-field terms; and (4) only near-field terms. Array radii, R, of 0.25, 0.5, 0.75, 1.0 and 2.0 are tested for each physical wave. The fault plane (2), which showed plain effects on physical waves, is selected because it causes less phase interference and surface waves dominate.

The accuracy of the source inversion, σ, is plotted in Figure 10. Despite the fact that σ for a complete half-space solution degrades as R decreases, σ for body waves becomes greatly improved in the ranges with small R. σ for far-field terms has much the same trend as that for near-field terms. Although a steeper slope for near-field terms is recognized, a good accuracy is not obtained in the case of $R = 0.25$ as expected from the steep trend. This graph implies body-wave analyses using near-source seismograms are very useful if there is little interference from surface waves. Note that surface waves are considerably dominant in our model fault. A differential array analysis using body-wave seismograms obtained from a source region (Spudich and Cranswick, 1984; Spudich and Oppenheimer, 1986) is another powerful way available for source studies. The technique is rather suitable for high frequencies, which are very difficult to process based upon usual source inversion frameworks. Since the technique makes use of a difference in arrival times of distinguishable phases, our method cannot be directly applied. Nevertheless, this simulation suggests the effectiveness of differential array analysis.

A previous study of differential array analysis, which used only far-field S waves (Iida *et al.*, 1986), showed that the desired array radius was approximately 0.5 to 1.0 (Fig. 11). In our current simulation of body waves, the best radius is 0.25 or smaller. A major factor for the difference is probably source complexity due to the number of subfaults and the rise time. Increasing source complexity seems to require a larger array radius.

5.3 Discussion

For an inclined fault bringing less phase interference, distant surface waves contribute most Subsidiary far-field body waves at distant stations are helpful in the absence of surface waves. As for a vertical fault generating more interference, on the other hand, far-field body waves observed at both near-source and distant stations are a sole contributor. "Contribution" means that the waves are not recoverable by any other waves, while "no contribution" means that they can be complemented by other waves. Also, station distribution able to avoid phase interference is highly desirable. Another important conclusion is that an array with a small array radius located in the source region would be useful provided that surface waves are suppressed and the source is not complex.

Invoking these results, we can discuss the adequacy of the half-space approximation. Certainly, Love waves are likely to bring further information at distant stations. However, as the Love-wave velocity is closer than the Rayleigh-wave velocity to S-wave velocity, phase interference between Love and S waves would be more severe, leading to speculation that the accuracy of the source inversion is not greatly improved by Love waves. While surface waves at distant stations are largely responsible for reducing the inversion uncertainty in the case of an inclined fault, far-field terms at small and large distances play a significant role in a vertical fault. Although we cannot give any direct guess on the influence of body waves that leave the source downgoing and are observed at distant stations, such waves appear to be more contaminated with surface waves since they have large travel times. That is, the effects of such waves at distant stations on the accuracy of the source inversion are not drastic. In conclusion, the half-space approximation is basically adequate.

Our physical wave simulations, together with other preceding studies on optimum array configurations (Iida *et al.*, 1988; Iida, 1990), suggest how results obtained from our idealized array geometries can be extrapolated to those actually used in the field. Because information obtained from distant surface waves cannot be recovered using any other waves, stations encircling the fault area with good azimuthal coverage are primarily required to unravel the source structure. These stations resolve the earlier stage of the rupturing process, while body waves in the source region resolve the later stage (Iida *et al.*, 1988). In the 1988 paper, we could not discriminate the effects of different physical waves. Using the concept of physical waves, we can have a better understanding of results in another previous paper, especially great dependence of the optimal array configuration on the fault mechanism (Iida, 1990). For a vertical strike-slip fault of strict phase requirements, stations immediately above the fault plane,

which are robust at the vertical resolution, are needed. In addition, some of the stations that form perfect azimuthal coverage give resolution of the source due to far-field body waves and/or surface waves On the other hand, an inclined dip-slip fault favors a grid pattern of stations that appears to help many phases to be separated.

6. REFERENCES

Aki, K. and P.G. Richards (1980). *Quantitative Seismology*, W.H. Freeman, Company, New York.

Anderson, J.G. and P G Silver (1985). Accelerogram evidence for southern rupture propagation on the Imperial fault during the October 15, 1979 earthquake, *Geophys. Res. Letters*, **12**, 349-352.

Anderson, J G., P. Bodin, J.N. Brune, J. Prince, S.K. Singh, R. Quaas and M Onate (1986). Strong ground motion from the Michoacan, Mexico, earthquake, *Science*, **233**, 1043-1049.

Archuleta, R.J. (1984). A faulting model for the 1979 Imperial Valley earthquake, *J. Geophys. Res.*, **89**, 4559-4585.

Backus, G.E. and J.F. Gilbert (1967) Numerical applications of a formalism for geophysical inverse problems, *Geophys. J.R. Astr. Soc.*, **13**, 247-276.

Beroza, G.C. and P. Spudich (1988). Linearized inversion for fault rupture behavior: application to the 1984 Morgan Hill, California, earthquake, *J. Geophys Res.*, **93B**, 6275-6296

Hartzell, S.H. and T.H. Heaton (1983). Inversion of strong ground motion and teleseismic waveform data for the rupture history of the 1979 Imperial Valley, California, earthquake, *Bull. Seism. Soc. Am.*, **73**, 1553-1583.

Hartzell, S. and M. Iida (1990). Source complexity of the 1987 Whittier Narrows, California, earthquake from the inversion of strong motion records, *J. Geophys Res.*, **95B**, 12475-12485.

Hasegawa, H.S. (1975). Seismic ground motion and residual deformation near a vertical fault, *Can. J. Earth Sci.*, **12**, 523-538.

Iida, M. (1990). Optimum strong-motion array geometry for source inversion - II, *Earthquake Eng. Struct. Dyn.*, **19**, 35-44.

Iida, M , T. Miyatake and K. Shimazaki (1986). Relationship between the accuracy on source inversion and array parameters, and their interpretation, *Proc 7th Japan Earthquake Eng. Symp.*, 451-456.

Iida, M., T. Miyatake and K. Shimazaki (1988). Optimum strong-motion array geometry for source inversion, *Earthquake Eng. Struct. Dyn.*, **16**, 1213-1225.

Iwan, W.D. (Editor) (1978). Strong-motion earthquake instrument array, *Proc. Internatl. Workshop on Strong-Motion Earthquake Instrument Arrays*, Honolulu, Hawaii.

Kawasaki, I., Y. Suzuki and R. Sato (1973). Seismic waves due to a shear fault in a semi-infinite media. Part I. Point source, *J. Phys. Earth*, **21**, 251-284.

Latham, G., P. Donoho, K. Griffiths, A. Roberts and A.K Ibraham (1978). The Texas ocean-bottom seismograph, *10th Offshore Technology Conference Proceedings*, **3**, 1467-1476.

Mendosa, C. and S.H. Hartzell (1989). Slip distribution of the 19 September 1985 Michoacan, Mexico, earthquake: near-source and teleseismic constraints, *Bull. Seism. Soc. Am.*, **79**, 655-669.

Menke, W. (1985). Imaging fault slip using teleseismic waveforms: analysis of a typical incomplete tomography problem, *Geophys. J.R. Astr. Soc.*, **81**, 197-204.

Miyatake, T., M. Iida and K. Shimazaki (1986). The effects of strong-motion array configuration on source inversion, *Bull. Seism Soc. Am.*, **76**, 1173-1185.

Mori, J. and K. Shimazaki (1985). Inversion of intermediate-period Rayleigh waves for source characteristics of the 1968 Tokachi-Oki earthquake, *J. Geophys. Res.*, **90**, 11374-11382.

Olson, A.H. and J.G. Anderson (1988). Implications of frequency-domain inversion of earthquake ground motions for resolving the space-time dependence of slip on the extended fault, *Geophys. J* , **94**, 443-455.

Olson, A.H. and R. Apsel (1982). Finite faults and inverse theory with applications to the 1979 Imperial Valley earthquake, *Bull. Seism. Soc. Am* , **72**, 1969-2001.

Spudich, P. and U. Ascher (1983). Calculation of complete theoretical seismograms in vertically varying media using collocation methods, *Geophys. J.R. Astr. Soc.*, **75**, 101-124.

Spudich, P. and E Cranswick (1984). Direct observation of rupture propagation during the 1979 Imperial Valley earthquake using a short baseline accelerometer array, *Bull. Seism. Soc. Am.*, **74**, 2083-2114.

Spudich, P and D. Oppenheimer (1986). Dense seismograph array observations of earthquake rupture dynamics, in *Earthquake Source Mechanics, Geophys. Monograph*, **37**, S. Das (Editor), 285-296.

Steinmetz, R.L., P.L. Donoho, J.D. Murff and G.V. Latham (1979). Soil coupling of a strong motion, ocean bottom seismometer, *11th Offshore Technology Conference Proceedings*, **4**, 2235-2249.

Steinmetz, R.L., J.D. Murff, G. Latham, A. Roberts, P. Donoho, L. Babb and T. Eichel (1981). Seismic instrumentation of the Kodiak shelf, *Marine Geotechnol.*, **4**, 192-221.

Tarantola, A and B. Valette (1982). Generalized nonlinear inverse problems solved using the least squares criterion, *Rev. Geophys. Space Phys.*, **20**, 219-232.

Wolberg, J.R. (1967). Prediction analysis, D. Van Nostrand Co., Inc., Princeton, New Jersey.

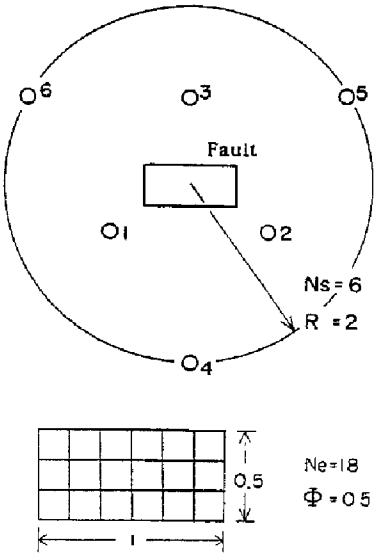

Fig. 1 Geometrical arrangement of fault planes and array stations for most simulations. Two kinds of faults are located at the center of an array: a pure strike-slip fault with a dip angle, $\delta = 90°$ and a pure dip-slip fault with $\delta = 30°$. All the distances are normalized by the fault length. The following are standard parameters (see Table 2). The number of subfaults, *Ne*, is 18 (16 x 3). The aspect ratio of the fault, Φ, is assumed to be 0.5. The depth of the top of the fault, *h*, is assumed as 0.1. The rupture is supposed to propagate unilaterally. The number of stations, *Ns*, is 6 and the array radius, *R*, is 2.0.

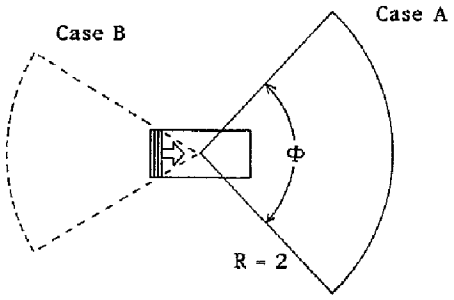

Fig. 2 Geometrical arrangement of fault planes and array stations for a simulation on azimuthal coverage of the source. The stations are distributed randomly in the fan-shaped area. We consider two cases as follows because *Ns* and ϕ can be interrelated. In the first case, the number of stations, *Ns*, is kept constant, but the density of stations is changed according to a change in azimuthal coverage, ϕ. In the second case, the number of stations, *Ns*, is kept proportional to the azimuthal coverage, ϕ. In this case, the density of stations is constant. Two sorts of unilateral rupture (in opposite directions), cases A and B are assumed. In case A, the rupture propagates toward the array. In case B, the rupture moves away from the array. See Figure 1 caption for detailed explanations on fault plane parameters.

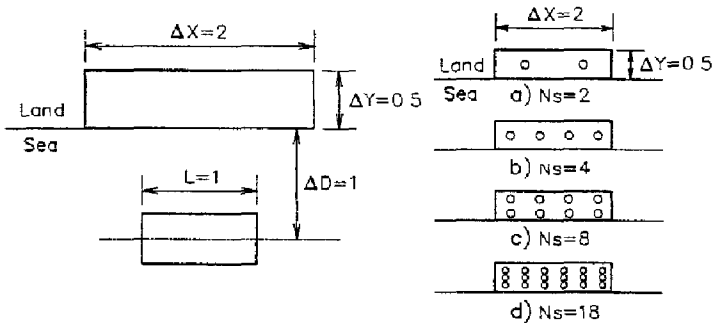

Fig. 3 Geometrical arrangement of fault planes and array stations for a simulation on an offshore subduction thrust. A pure dip-slip fault with a dip angle, $\delta = 30°$ is assumed. The numbers of surface stations and ocean bottom stations, *Ns* and *No*, are varied separately to estimate their influence. The distribution in the surface stations is fixed based upon the number of surface stations, *Ns*, and forms a line or a rectangular grid, as illustrated. Several patterns of ocean bottom stations are tested for each pair of *Ns* and *No*. See Figure 1 caption for detailed explanations on fault plane parameters.

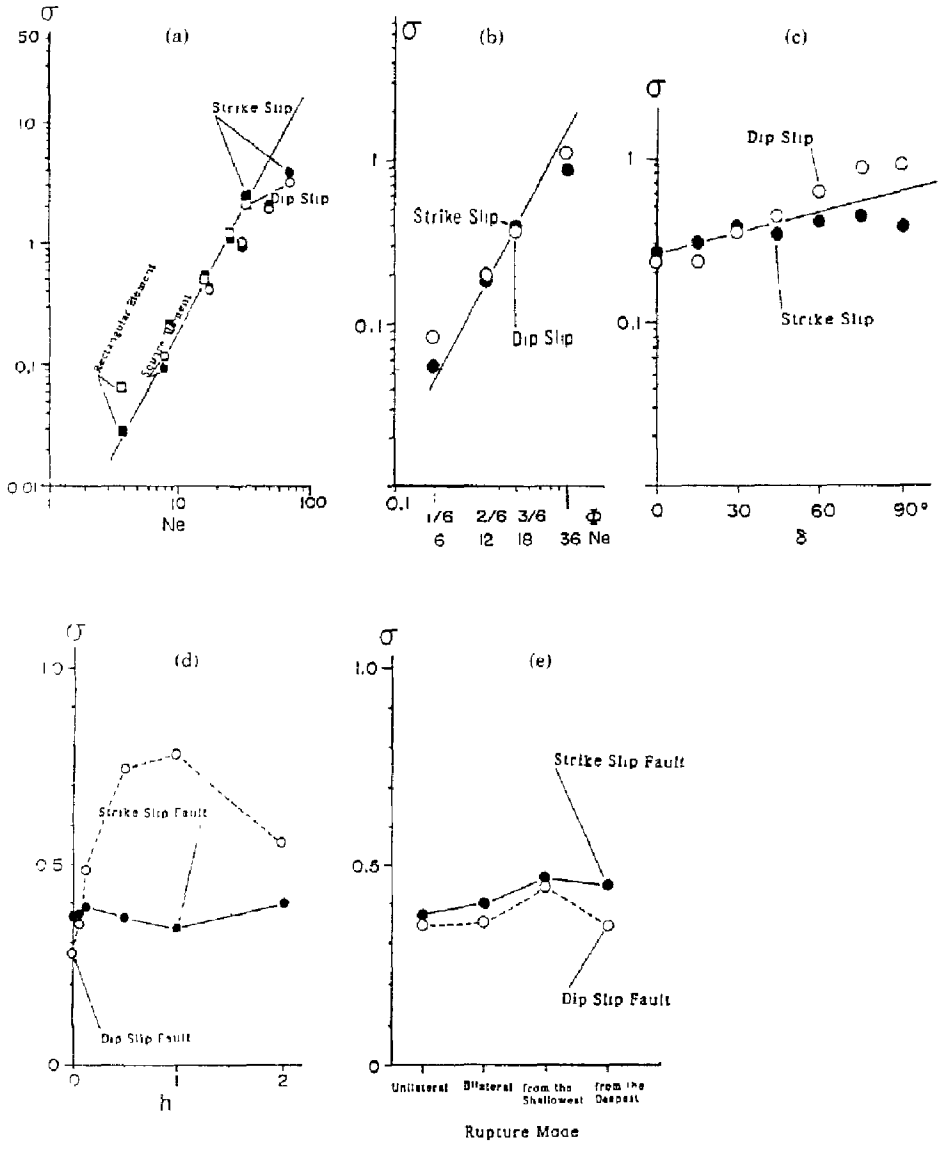

Fig. 4 Relationship between the inversion uncertainty, σ, and fault parameters (see the number of subfaults, *Ne*, the aspect ratio, Φ, the dip angle, δ, the fault depth, h, and the rupture mode). Please note that the ordinate is in linear scale in (d) and (e).

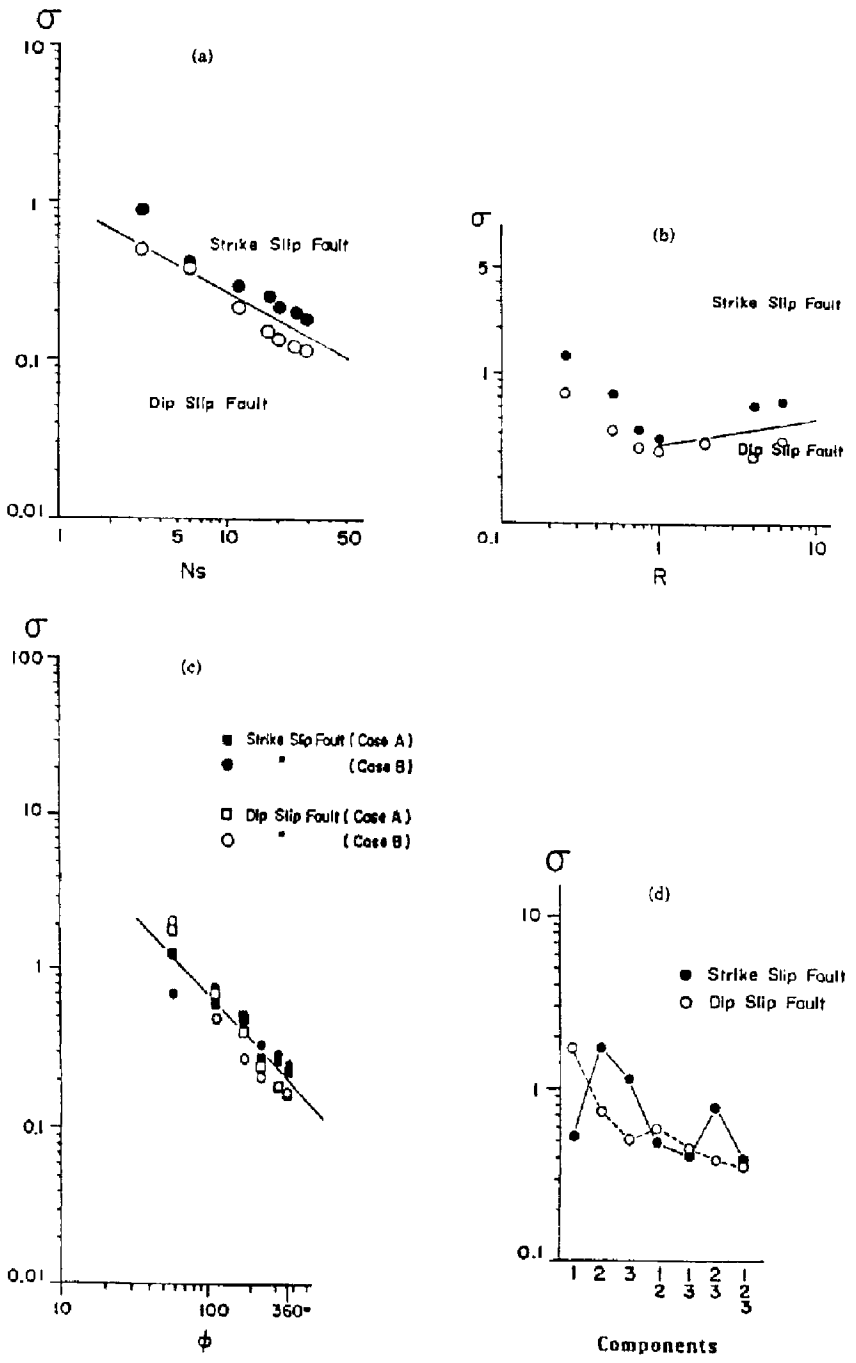

Fig. 5 Relationship between the inversion uncertainty, σ, and array parameters (the number of stations, *Ns*, the array radius, *R*, the azimuthal coverage, ϕ, and the components of the seismograms). In (c), only the result for a case that *Ns* is kept proportional to ϕ is shown. In (d), 1 means the component parallel to the fault strike, 2 refers to the horizontal component perpendicular to the fault strike, and 3 is the vertical component.

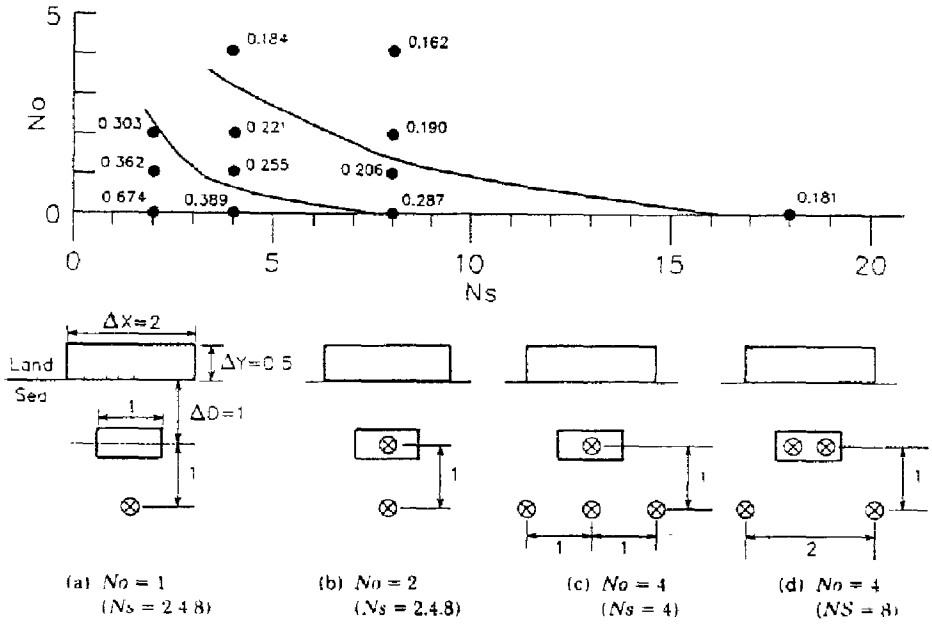

Fig. 6 Relationship among the inversion uncertainty, σ, the numbers of surface stations and ocean bottom stations, *Ns* and *No*, obtained from an offshore subduction thrust simulation. The best positions of ocean bottom stations are depicted for each pair of *Ns* and *No*. We find that, when one or two ocean bottom seismographs are installed, the locations are not dependent on the number of surface stations, *Ns*, whereas the locations are changed according to *Ns* in the case of four ocean bottom seismographs.

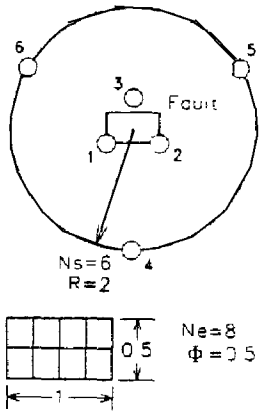

Fig 7 Geometrical arrangement of fault planes and array stations for studying effects of various physical waves. Basically, this is the same as that shown in Figure 1, except that *Ne* is 8 (4 x 2), and stations 1 to 3 are shifted toward the center of the station array in order that the distance between each station and the center of the array is halved.

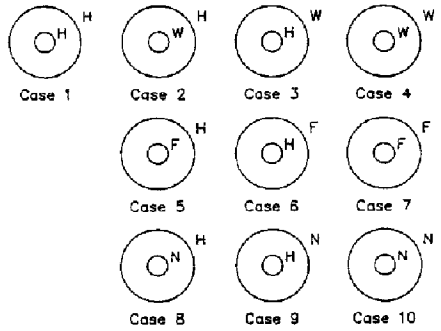

Fig. 8 Schematic plot clarifying the types of physical waves used at each station. The inner circle represents three near-fault stations, while the outer circle shows other three distant stations. H = complete half-space seismograms are used; W = complete wholespace seismograms are used, so surface waves are removed. F and N = only far-field or near-field terms for the wholespace seismograms are used ($W = F + N$).

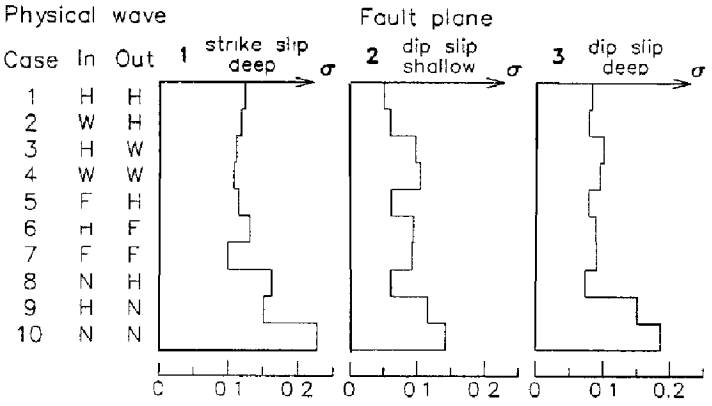

Fig. 9 The accuracy of the source inversion for different fault planes and various physical waves. See Table 3 for the fault planes and Figure 8 for the physical waves.

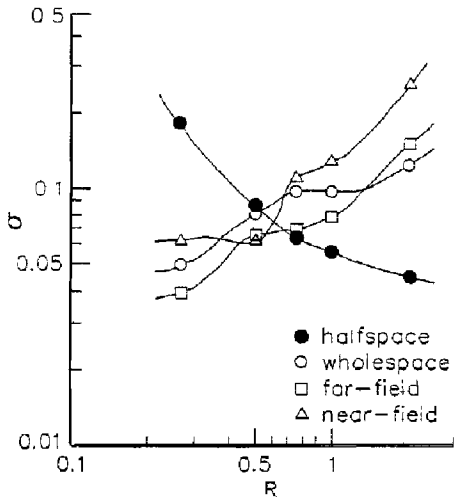

Fig 10 Relationship between the inversion uncertainty, σ, and the array radius, R, for different physical waves. The solid circle, open circle, square, and triangle mean that a complete half-space solution, a complete wholespace solution, only far-field terms, and only near-field terms are used, respectively. A shallower inclined dip-slip fault is used.

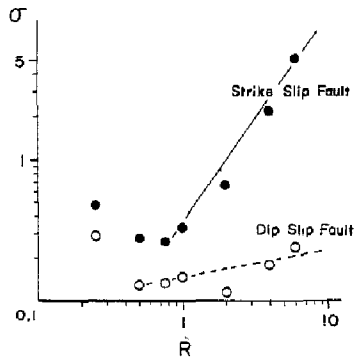

Fig. 11 Relationship between the inversion uncertainty, σ, and the array radius, R, when only far-field S waves are used.

Lecture 2 ARRAY LAYOUT FOR SOURCE INVERSION
Subject 2 Optimum Strong-Motion Array Geometry for Source Inversion

1. INTRODUCTION

This study is a revised version of optimizing strong-motion array geometry for source inversions. As was stated in our previous study,[1] the question of how we quantitatively estimate effects of strong-motion array geometry had not explicitly been addressed, until two different numerical approaches were tried for this problem.[1,3] One approach estimated the accuracy of a source inversion on the basis of Wolberg's prediction analysis for each of a number of fault-array combinations.[1] The other approach evaluated the effect of recording geometries on the retrieval of source information using a frequency-domain inversion and a minimum norm solution.[3] It should be recognized throughout these studies that the reliability of the analytical results is inevitably governed by the array geometry.

Understanding of the nature of earthquake ground motion is a crucial problem to be solved from both strong-motion seismology and earthquake engineering points of view, and in particular, the estimation of strong ground motions at an arbitrary site is the least understood problem in the field of earthquake engineering. Much information on the detailed source and structure effects and on the wide variety of local conditions is undoubtedly necessary. To date, many inverse studies have been done to evaluate parameters related to earthquake sources and crustal and site structures. Considering the large variations in the results recognized among such inverse studies, however, a systematic estimate for the accuracy of inversion solutions is required. In addition, despite recent developments in the methodology of data analysis and the performance of seismographs, which have made prominent improvements in the accuracy of inversion solutions, virtually very little is known about the effectiveness of array geometries

As a first step, we investigated the effects of array geometry on source inversion in our previous study.[1] The optimum strong-motion array geometry for each of three types of earthquake faults, strike-slip, dip-slip and offshore subduction thrust, was determined on the basis of the ability to estimate the seismic moments of subfault elements. 'Optimum' means that the solution of a source inversion becomes the most accurate for the same number of array stations and for the same process of a fault rupture. The resultant optimum array geometries were compared with the ones proposed on the basis of empirical judgement at the International Workshop on Strong-Motion Earthquake Instrument Arrays held in Honolulu, Hawaii in 1978.[2] The results were not necessarily consistent.

The most serious omission noted in the previous study[1] appears to be use of only the far-field S waves, ignoring P and surface waves and the near-field terms in the Green's function. Effects of these waves should be considered in the light of a realistic array design. The effectiveness of a complete Green's function in a half-space[4] was a systematically examined in another study.[5] The results indicated that the accuracy of the source inversion was much less dependent on array parameters for the complete solution than for the S-wave solution. This suggested that the simultaneous use of several kinds of waves[6,7] was advantageous in source inversion studies.

Accordingly, optimum strong-motion array geometries for source inversions are again determined for the same three types of earthquake faults, using an improved method based upon the complete wave solution. The optimum array geometries determined here are compared with the ones obtained in the previous study[1] and/or the ones proposed at the International Workshop.[2]

2. METHODS

---

* This lecture note is based on the paper of the same title written by Masahiro Iida, published on "Earthquake Engineering and Structural Dynamics, Vol. 19, 35-44 (1990)".

The method is the same as the one used in the previous study.[1] We briefly describe the technique. The only distinctive improvement is the employment of a complete Green's function in a half-space.[4] Certainly, this Green's function does not include the specification of heterogeneous structure, and the use of a more complete Green's function is feasible in principle. At present, however, it requires excessive computational efforts.

We use Wolberg's prediction analysis to calculate the accuracy of a waveform source inversion; that is, we estimate the accuracy of the solution from errors in the data by using a principle of error propagation. Most of the current source inversion studies deal with a detailed history of rupture on a fault. We divide the entire fault into many subfaults and use the displacement waveform representation for each subfault. A common, simple source time function which depends upon the subfault size is assumed for each subfault. The seismic moment and the rupture onset time for each subfault are unknown parameters, as is generally the case in source inversion studies. The unknown parameters are determined using a least-squares criterion. Here, un certainties are assumed for several independent variables. We define the accuracy of the source inversion, σ, by the maximum standard deviation of errors in estimating the seismic moment for each subfault, which is normalized by the seismic moment.

The theoretical waveform is a function of known and unknown parameters. The known parameters whose uncertainties are taken into account (the dip angle, the strike direction, the slip angle, the wave amplitude and the arrival time) are regarded as the independent variables and are denoted by x_p ($p = 1,\ldots, Np$). We denote by a_i ($i = 1,\ldots,Nu$) the unknown parameters, the seismic moment and rupture onset time for each subfault. The wave amplitude for the jth time point at the kth station is expressed as $u^k(t_j) = f_j^k(x_{1kj},\ldots,x_{Npkj}; a_1,\ldots,a_{Nu})$. Two residuals, Ru_{kj} and Rx_{pkj}, are defined as the differences between the observed and calculated values:

$$Ru_{kj} = U^k(t_j) - u^k(t_j)$$

$$Rx_{pkj} = X_{pkj} - x_{pkj}$$

where we denote by $U(t_j)$ and X_{pkj} ($p = 1,\ldots,Np$) the observed wave amplitude and the true values for known parameters, respectively. A least-squares method is used to determine the values of unknown parameters a_i ($i = 1,\ldots, Nu$), which minimize the weighted sum of the squares of the residuals, S.

$$S = \sum_k \sum_j \left(Wu_{kj}\, Ru_{kj}^2 + \sum_p^{Np} Wx_{pkj}\, Rx_{pkj}^2 \right)$$

where $Wu_{kj} = 1/\sigma u_{kj}^2$ and $Wx_{pkj} = 1/\sigma x_{pkj}^2$. We denote the standard deviation of errors in wave amplitude by σu_{kj} and that in known parameters by σx_{pkj}. The solution for a general least-squares problem is obtained by solving normal equations in matrix form. If we follow Wolberg's prediction analysis, the standard deviation of errors in the ith unknown parameter σa_i can be estimated by calculating an inverse of the matrix and it is unnecessary to solve the actual normal equations.

The near-field terms and P and surface waves included in the complete solution have complex effects that are difficult to predict. They will complicate the waveforms and result in an increase in the uncertainty of the solution. On the other hand, the increase in the source information contained in the waveforms will decrease the uncertainty. A direct comparison of the absolute values between the results for the complete solution and the S-wave solution[1] cannot be expected because of the following three differences in the calculations. First, using the same time interval, the exact solution needs more data as it involves a series of waves from P to surface waves. Secondly, a ramp function is assumed as the source time function in the case of the complete solution (because of the simplification and computational time), although a slightly more complex function was used in the case of the S-wave solution. Thirdly, attenuation was considered by assuming an exponential decay of the S-wave amplitude with distance for the S-wave solution. Since a simple, appropriate structural uncertainty is difficult to incorporate in the case of the complete solution, timing errors of $\delta t = |\delta v/v|\, t$ are introduced, where t is the measured time from the start of the fault fracture process, v is the wave propagation velocity and δv is the error in the velocity.

Here, 0.05 (5 percent error) is adopted for $|\delta v/v|$. This assumption signifies that the timing errors due to unknown structures (e.g. interference with different phases and distorted waveform during wave propagation) increase with increasing time from the rupture initiation and increasing epicentral distance. This representation effectively expresses the spatio-temporal disturbance of wave propagation due to unknown structures.

Assumption of the same values for fault parameters as those used in the previous study[1] facilitates the comparison of the obtained results not only with the previous ones but also with the ones addressed at the Workshop. Three assumed types of fault geometries are pictured in Figure 1. The tabulated information on fault parameters is shown in Table I. They are fixed as the same values as in the previous study with the exception of a few parameters relating to wave propagation.

Table I. Parameters assumed for investigating effects of array configurations on a source inversion

	Strike–slip	Dip–slip	Subduction thrust
Fault area	90 km × 15 km	45 km × 15 km	90 km × 45 km
Number of fault elements, *Ne*	24(= 12 × 2)	12(= 6 × 2)	18(= 6 × 3)
Subfault area	7·5 km × 7·5 km	7·5 km × 7·5 km	15 km × 15 km
Dip angle, δ	90°	45°	30°
Final offset, *D*	2·0 m	1·0 m	3·0 m
Rise time, τ	8·4 sec	8·4 sec	14·4 sec
Rupture mode	unilateral	unilateral	unilateral
Rupture velocity, V_r	2·5 km/sec	2·5 km/sec	2·5 km/sec
Depth to top of fault, *h*	3 km	3 km	9 km
P-wave velocity, V_p	5·0 km/sec	5·0 km/sec	5·0 km/sec
S-wave velocity, V_s	3·0 km/sec	3·0 km/sec	3·0 km/sec

By assuming a unilateral mode of fault rupture and by fixing the number of array stations at 16, the optimum array configuration is evaluated by trial and error modelling for each of the three fault geometries shown in Figure 1. A wide variety of array configurations is tested for their respective fault geometries. The array configurations examined for a strike-slip fault, a dip-slip fault and an offshore subduction thrust fault are shown in Figures 2, 3 and 4, respectively.

3. RESULTS AND DISCUSSION

The numerical value corresponding to each array configuration in Figures 2, 3 and 4 shows the accuracy of the source inversion, σ; in other words, the maximum standard deviation of errors in estimating the seismic moment for each subfault, normalized by the seismic moment. For example, 0.244 in Figure 2 means 24.4 percent error. Figures 2 and 3 show the array configuration effects for strike-slip and dip-slip faults. The dominant factor on array configuration for a strike-slip fault is found to be good azimuthal coverage of stations [Cases (g) and (h)], and stations close to the fault [Cases (k) and (l)]. A perpendicular array to the fault strike [Case (d)] can give reasonable results. Satisfactory solutions are difficult using only array stations aligned parallel to the fault trace [Cases (a) and (b)]. Arrays that include no near-fault stations [Cases (i) and (j)], and T-shaped [Case (c)] or grid-shaped [Cases (e) and (f)] arrays give poor results as well.

Effective array configurations for a dip-slip fault include stations parallel and close to the fault [Cases (a) and (b)] or a grid-shaped pattern [Cases (e) and (f)]. A T-shaped array [Case (c)] or good azimuthal coverage [Cases (k) and (l)] also provide reasonable solutions. Lack of near-fault stations paralleling the fault does a poorer job of resolving the rupture details [Cases (d) and (g) to (j)].

A significant improvement of the uncertainty of the solution due to strong-motion ocean bottom stations is seen in Figure 4, where effects of the array configuration for an offshore subduction thrust fault are evaluated [Cases (g) to (l)]. Little dependency of the uncertainty on the array configuration is attributed to the various restricted station installations on the land area [Cases (a) to (f)], although a few lines of array stations aligned along the shoreline appear to be slightly better than others.

After some additional simulations on other array configurations for each of these earthquake faults, a preferred array configuration for each fault geometry is presented in Figure 5 together with the corresponding distribution of the standard deviations of errors in estimating the seismic moments over the fault surface. We find that the distribution of the estimation errors is generally uniform over the fault surface for the preferred array configurations. The preferred array configurations are compared with both those obtained in the previous study[1] (Figure 6), where the same kind of quantitative estimation was done using only the far-field S waves, and the ones proposed on the basis of empirical judgement at the 1978 International Workshop[2] (Figure 7). The preferred array configuration obtained here for a strike-slip fault looks similar to the previous study [Figure 6 (a)]. The array configuration appears to bear less resemblance to the comb-shaped one which was recommended at the Workshop [Figure 7(a)]. The optimum array for a dip-slip fault, a grid pattern, seems substantially different from the previous study [Figure 6(b)]. We should note that this configuration is the same as the one recommended at the Workshop [Figure 7(b)]. For an offshore subduction thrust fault, the preferred configuration is much the same as the previous study [Figure 6(c)], and it also is similar to the Workshop proposal [Figure 7(c)]. The ocean bottom stations do not affect the desired array configuration on the land area.

The large variation in the uncertainty of the solution due to the difference in array configuration for the strike-slip fault, which was found in the previous study [Figure 6(a)], is not seen in the present study (Figure 2). It is probably because a stable inversion is performed through a complete Green's function. Inclusion of the near-field terms and P and surface waves causes less dependency of the accuracy of the source inversion on fault-array parameters, emphasizing the advantages of using different kind of waves.[5] Presumably, the importance of distant stations for a strike-slip fault is associated with a contribution due to surface waves. Surface waves are also helpful for carrying out the source inversion in the absence of near-fault stations for an offshore fault. On the other hand, near-fault stations play a more important role for a dip-slip event. This fact suggests that a complicated displacement field around the source area caused by the dip-slip event can be discriminated efficiently with a combination of different waves. The present results are not designed for detailed discussion because of the imperfect method[1] and the Green's function used, but provide a general description as to the array layout suitable for source studies.

Finally, it should be mentioned that complex effects due to crustal structure, which are very difficult to parameterize in a standard format, are not taken into account in the present study. The effects possibly produce much more uncertainty for seismograms recorded at distant stations than for those at nearby stations beyond the assumption of $\delta t = |\delta v/v| t$. Near-fault stations are important for source studies, so that installation of ocean bottom instruments is required for an offshore event.

4. CONCLUSIONS

Optimum array geometry for source inversions has been investigated using a complete Green's function in a homogeneous half-space. Three earthquake faults considered are strike-slip, dip-slip and offshore thrust faults. The preferred array geometries quantitatively determined have been compared with the ones previously obtained using only the far-field S waves[1] and the ones proposed on the basis of empirical judgement at the 1978 International Workshop on Strong-Motion Earthquake Instrument Arrays.[2] The main results are summarized as follows.

1) Use of a complete Green's function reduces the dependency on the array configuration. This suggests that the simultaneous use of different kinds of waves in source studies is desirable.

2) The optimum strong-motion array for a strike-slip fault is characterized by stations well spaced in azimuth,

together with near-fault stations. The optimum array for a dip-slip event has stations arranged in a grid-shaped form located in the near-source region. The installation of ocean bottom stations is desirable for an offshore event.

3) The optimum strong-motion array geometries which have been derived from the use of a complete Green's function are generally consistent with the ones proposed at the 1978 International Workshop.

5. REFERENCES

1. Iida, M., T. Miyatake and K. Shimazaki (1988). Optimum strong-motion array geometry for source inversion, *Earthquake Eng. Struct. Dyn.*, **16**, 1213-1225.

2. Iwan, W.D. (Editor) (1978). Strong-motion earthquake instrument array, *Proc. Int. workshop strong-motion earthquake instrument arrays*, Honolulu, Hawaii.

3. Olson, A.H. and J.G. Anderson (1988). Implications of frequency-domain inversion of earthquake ground motions for resolving the space-time dependence of slip on an extended fault, *Geophys. J.*, **94**, 443-455.

4. Kawasaki, I., Y. Suzuki and R. Sato (1973). Seismic waves due to a shear fault in a semi-infinite medium, Part I: Point source, *J. Phys. Earth*, **21**, 251-284.

5. Iida, M., T. Miyatake and K. Shimazaki (submitted for publication). Relationship between strong-motion array parameters and the accuracy of source inversion, *Bull. Seism. Soc. Am.* (submitted for publication)

6. Olson, A.H. and R Apsel (1982). Finite faults and inverse theory with applications to the 1979 Imperial Valley earthquake, *Bull. Seism. Soc. Am.*, **72**, 1969-2001.

7. Hartzell, S.H. and T.H. Heaton (1983). Inversion of strong ground motion and teleseismic waveform data for the rupture history of the 1979 Imperial Valley, California, earthquake, *Bull. Seism. Soc. Am.*, **73**, 1553-1583.

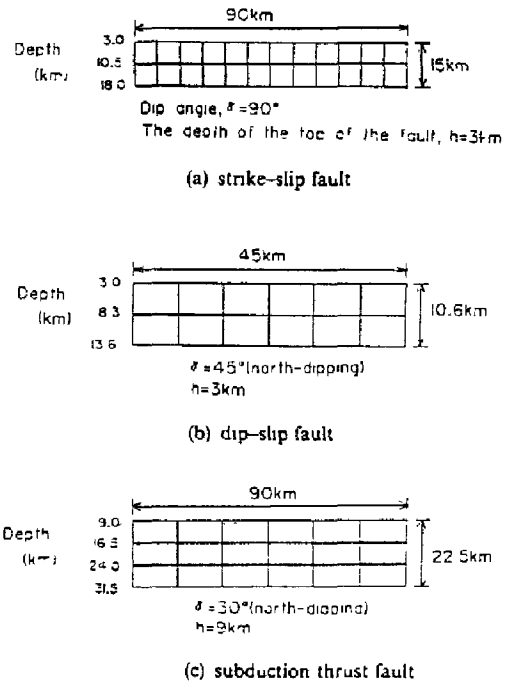

Fig. 1 Types of fault geometries used for investigating effects of array configurations on source inversions (cross sections): (a) strike-slip; (b) dip-slip; (c) subduction thrust fault

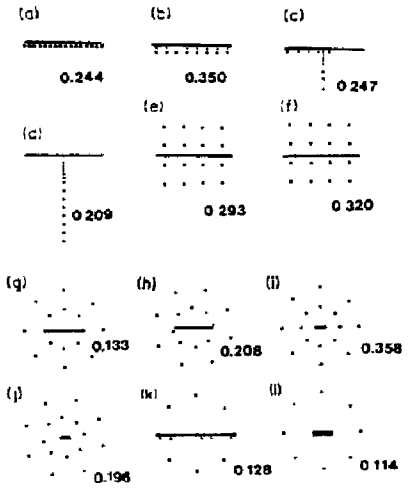

Fig. 2 Array configurations (plan views) tested for investigation of the optimum configuration for a strike-slip fault. The horizontal bar shows the fault and the dots indicate stations. The numerical value indicates the accuracy of the inversion solution, σ, the maximum standard deviation of errors in estimating the seismic moment for each subfault, normalized by the seismic moment. For example, 0.244 means 24.4 per cent error.